

Interaction of Gravity Forces in Spot GTA Weld Pool

Both experimental and numerical results showed that the depth of the weld zone decreases substantially by increasing the gravity level

BY A. BAHRAMI, D. K. AIDUN, AND D. T. VALENTINE

ABSTRACT

The interaction of convective forces in the weld pool of spot gas tungsten arc (GTA) welding of AISI 1018 steel was examined experimentally and numerically in this research work. To alter the effect of buoyancy convection in the weld pool, the multigravity research welding system (MGRWS) was used to investigate high-gravity conditions during the welding process. Thus, we were able to examine the interaction of buoyancy convection with Marangoni effect and Lorentz force; this interaction determines the penetration of the weld. Different welding conditions were simulated numerically using the finite-element analysis software *COMSOL Multiphysics*. This software allowed calculation of the fluid flow and heat transfer in the weld pool as a function of gravity level. The numerical results of the weld geometry showed reasonable agreement with the experimental data. The results show that the depth of penetration and the size of the weld zone decrease as the gravity increases. However, for gravity levels greater than 4g the changes in the depth and width of the weld zone were found to be negligible.

(Refs. 4, 13) studied fluid flow and heat transfer in welding of AISI 1005 low-carbon steel. Due to lower surface tension temperature derivative and higher electrical conductivity of low-carbon steel as compared to stainless steel, the geometry of the WZ for low-carbon steels is totally different from that of austenitic stainless steels.

Domey et al. (Ref. 14) simulated the effect of gravity on WP shape in 6061 Al alloy. They showed that increasing gravity decreases depth of the WZ. Aidun et al. (Ref. 1) experimentally investigated the effect of gravity for the GTA and gas metal arc (GMA) welding processes of 304 stainless steels. They also investigated the effect of enhanced gravity on microstructure of an Al-Cu-Li weld (Ref. 15). They showed that the unmixed zone becomes smaller as a result of increase in buoyancy convection.

The general scope of this research work is to provide enhanced insight into the role of gravity-induced convection on the size and shape of the WZ in GTA welding. Fluid flow and heat transfer in the workpiece during melting were modeled numerically to examine different gravity (g) levels for 1018 low-carbon steel. A set of physical spot GTA tests was performed for several g-levels in the multigravity research welding system (MGRWS). The samples were sectioned, polished, and etched to determine the WZ profiles. The WZ profiles obtained from the numerical model are compared to the same determined experimentally. The comparisons illustrate that the numerical predictions are in reasonable agreement with the experimental results. In this paper we show how the interaction between Marangoni, Lorentz, and buoyancy convective forces in the WP influence the aspect ratio of the WZ.

Computational Methodology

The GTA welding process on low-carbon steel coupons under different gravity levels are considered in this study. Schematic representation of the geometry

Introduction

Investigation of fluid flow and heat transfer in the welding process is necessary in order to predict important factors such as weld zone (WZ) and heat-affected zone (HAZ) shape/size, cooling rate, thermal stresses, and possibly formation of defects. Beside the Marangoni effect and electromagnetic forces, gravity-driven buoyancy-induced flow is one of the major factors that drive the flow of molten metal in the weld pool (WP). This buoyancy force, depending on the mass-density variation in the pool, can reduce or enhance the Marangoni and electromagnetic effects (Ref. 1).

Many studies have been conducted in the last few decades to investigate the fluid flow and heat transfer numerically and experimentally in welding processes, especially for gas tungsten arc welding (GTAW). Researchers numerically modeled this welding process either separately from the arc by assuming a heat flux and a current density distribution on the top sur-

face of the WP (Refs. 2–6) or in a unified system with the arc (Refs. 7–10). The latter models were applied to study the effect of gas pressure and drag force on the surface of the WP.

Some researchers studied transport phenomena in completely penetrated welding by including the effect of surface tension at the bottom of the WP (Refs. 3, 6). Modeling of pulsed current GTA welding also has been studied (Refs. 11, 12). These researchers concluded that implementation of pulsed current can improve stability of the arc and reduce thermal distortion.

Many researchers examined the welding of AISI 304 stainless steel. Zhang et al.

KEYWORDS

Gas Tungsten Arc Welding (GTAW)
Weld Pool
High Gravity
Convective Forces
Buoyancy
Marangoni Effect
Lorentz Force
Fluid Flow
Heat Transfer

A. BAHRAMI (bahrama@clarkson.edu) is a PhD candidate; D. K. AIDUN is professor and chair of the Mechanical and Aeronautical Engineering (MAE) Dept., and D. T. VALENTINE is associate professor in the MAE Dept. at Clarkson University, Potsdam, N.Y.

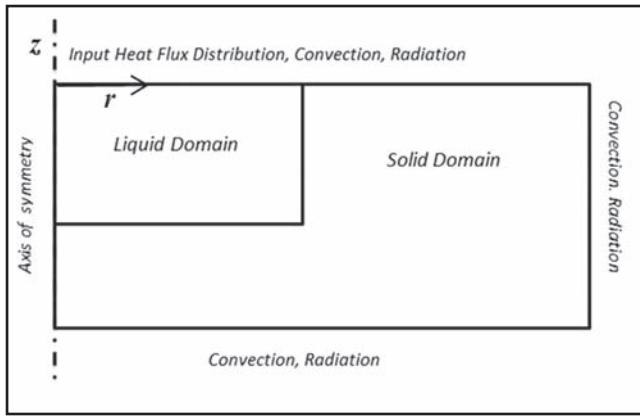


Fig. 1 — Schematic of the domain of the study and applied boundary condition.

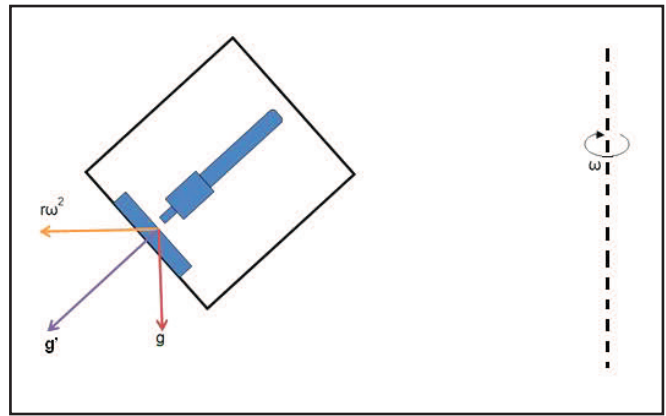


Fig. 2 — Schematic of the welding box.

of the model is shown in Fig. 1.

The following assumptions are made in constructing the mathematical model:

1. The model studies a spot GTA weld of similar metals; therefore, an axial-symmetric geometry is applied.
2. The flow pattern in the weld pool is laminar and incompressible.
3. The Boussinesq approximation is applied to simulate buoyancy-induced convection.
4. All properties of the liquid metal, other than its surface tension and the difference in mass-density associated with the buoyancy force, are independent of temperature.
5. The base metal is initially at ambient temperature.
6. Gaussian distributions are used to simulate the arc current density and heat flux.

The computational model includes

phase change, fluid flow, heat transfer, and electromagnetics. The equations solved numerically are conservation of mass, conservation of momentum, and conservation of energy along with classic Maxwell's equations for electromagnetism; they are described in detail in the literature (Refs. 1–7).

The buoyancy force is associated with gradients in the WP mass density. This force and the electromagnetic force (Lorentz force) are volume forces that are sources of momentum in the equations of motion. The interface between the solid and liquid phases was modeled by applying the Carman-Kozeny theory described in Refs. 16–18. Beside the solid to liquid phase change, which occurs in any GTAW process, the arc time in the present study is sufficiently long to cause a very small amount of metal vaporization. The enthalpies of fusion and vaporization are incorporated into the specific heat of the liq-

uid as was done by others in previous investigations (Refs. 7, 19).

Mathematical Model

In this research, the high-gravity accelerations are generated by using a rotating system (details of the system are explained in the experimental procedure section). The experimental setup was designed such that the resultant of the gravitational and centrifugal forces is always perpendicular to the sample as illustrated in Fig. 2. Beside the centrifugal force that is superimposed on the gravity (g) force, a Coriolis force is also generated in a rotating system because the coordinates that are typically selected rotate with the object of interest. In order to take into account the effects of rotation, the gravity vector in the momentum equation is replaced by the resultant of the gravity and the centrifugal force, which is called, g' in Fig. 2. The Coriolis effect imposes a body force equal to $-2\Omega \times \vec{u}$ that acts on the fluid (Ref. 20).

The relative importance of the Coriolis effect in this research is determined by nondimensionalization of the momentum equation in a rotating coordinate system. The parameters used to write the momentum equation in dimensionless form are the effective arc radius for the length scale, the kinematic viscosity divided by the arc radius for the velocity scale, and the difference in temperature described below, viz.,

$$\left(\frac{\partial \vec{u}^*}{\partial t^*} + \vec{u}^* \cdot \nabla \vec{u}^* \right) = -\nabla P^* + \nabla^2 \vec{u}^* + Gr \theta + Rm \left(\vec{j}^* \times \vec{B}^* \right) + K^* \vec{u}^* - \frac{1}{Ro} \Omega^* \times \vec{u}^* \quad (1)$$

where u^* , t^* , P^* , θ , j^* , B^* , and Ω^* are di-

Table 1 — Thermophysical Properties and Arc Parameters Used in the Numerical Simulation

Property Name	Value
Ambient temperature	293K
Liquidus temperature	1802 K (Ref. 25)
Solidus temperature	1770 K (Ref. 25)
Boiling temperature	3200 K (Ref. 26)
Heat of fusion	240 kJ/kg (Ref. 25)
Heat of vaporization	6340 kJ/kg (Ref. 26)
Solid specific heat	750 J/kgK (Ref. 25)
Liquid specific heat	840 J/kgK (Ref. 25)
Solid thermal conductivity	39.4 W/mK (Ref. 25)
Liquid thermal conductivity	36.5 W/mK (Ref. 25)
Solid density	7530 kg/m ³ (Ref. 25)
Liquid density	7150 kg/m ³ (Ref. 25)
Volume thermal expansion of liquid	$1.2 \times 10^{-4} / K$ (Ref. 25)
Dynamic viscosity	$6.3 \times 10^{-3} \text{ kg/(m.s)}$ (Ref. 25)
Effective radius of current density distribution	4.5 mm
Effective radius of heat source	3.5 mm
Vacuum permeability	$4\pi \times 10^{-7} \text{ N/A}^2$
Convective heat transfer coefficient	20 W/m ² K
Surface emissivity	0.75
Arc efficiency	75% (Calibrated with experiment at 1 g)

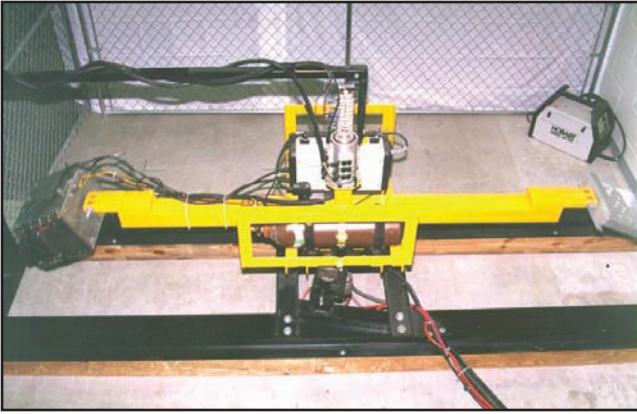


Fig. 3 — Multigravity research welding system (MGRWS).

dimensionless velocity, time, pressure, temperature, current density, magnetic field, and rotational velocity of the MGRWS. The parameter K^* is the dimensionless source coefficient, which is used to determine the interface between the solid and liquid phases as described in Ref. 19; in the liquid phase (\tilde{u}^*) is finite and K^* is zero. The dimensionless numbers, Gr , Rm , and Ro , denote Grashof (buoyancy to viscous forces), Magnetic Reynolds (electromagnetic to viscous force), and Rossby (viscous to Coriolis force) numbers, respectively, and are defined as follows:

$$Gr = \frac{\beta \Delta T L^3 g}{\nu^2}$$

$$Rm = \frac{\mu_0 I^2}{\pi^2 \rho_l \nu^2}$$

$$Ro = \frac{\nu}{2L^2 \omega}$$

In these dimensionless groups, β , ν , ρ_l , g , μ_0 , and I are volumetric thermal expansion, kinematic viscosity, liquid metal density, gravitational acceleration, vacuum permeability, and arc current, respectively. The effective radius, L , of the arc is also applied in the correlation of input heat flux distribution. The overall temperature difference ΔT in Gr is the difference of vaporization and liquidus temperature. A representative size of the angular velocity, ω , used in this study is 6.28 rad/s, which simulates the gravity of 4.5 g; this is the angular velocity used to compute the dimensionless parameters that characterize the problems investigated in this research.

Applying these scales, we obtained the following values of the dimensionless parameters: $Gr \approx 2 \times 10^5$, and $Rm \approx 5 \times 10^5$, and

$$Ro \approx 0.01 \rightarrow \frac{1}{Ro} \approx 10^2$$

The dimensional analysis shows that the Coriolis effect ($1/Ro \sim 10^2$) in Equation 1 is far less than the effect of buoyancy and the Lorentz force, thus the Coriolis effect was neglected in the numerical simulations. Neglecting the Coriolis effect made it possible to utilize an axial-symmetric geometry model.

Boundary Conditions

A two-dimensional axial-symmetric domain is selected to simulate the welding process in this study. Figure 1 provides a schematic of the domains and the boundary conditions along the r-z coordinates.

For the electromagnetic boundary conditions, a Gaussian normal current density distribution is applied at the top surface of the base metal (BM) to simulate the current density input from the arc (Ref. 21). It is as follows:

$$j(r) = \frac{3I}{\pi r_i^2} \exp\left(\frac{-3r^2}{r_i^2}\right) \tag{2}$$

where I is the electric current and r_i is the effective radius of the current density distribution. The bottom surface of the BM domain is the ground and all the other boundaries are considered as electrically

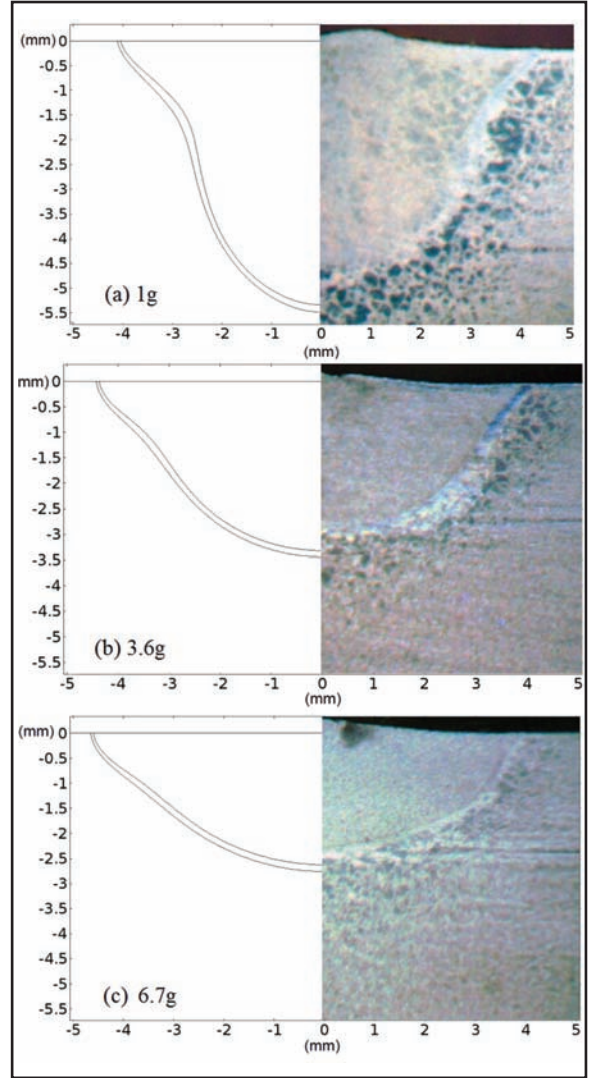


Fig. 4 — Comparison of the weld zone profile of the experiment and the numerical simulation.

and magnetically insulated.

For the fluid flow, the flow velocity is zero at all the boundaries other than along the top surface. At the top surface, as a result of changes in the surface tension of the melt as a function of temperature, a surface Marangoni force drives the flow. This effect is applied as a surface stress boundary condition. Surface tension in molten Fe-S alloys is known to be a function of temperature and sulfur activity. The equation correlated by Sahoo et al. (Refs. 22, 23) for the temperature gradient of surface tension is applied in this investigation.

Table 2 — Composition of 1018 Steel

	Fe	C (wt-%)	Mn (wt-%)	Si (wt-%)	P (wt-%)	S (wt-%)
1018	Bal	0.15–0.20	0.60–0.90	0.15–0.30	<0.04	<0.03

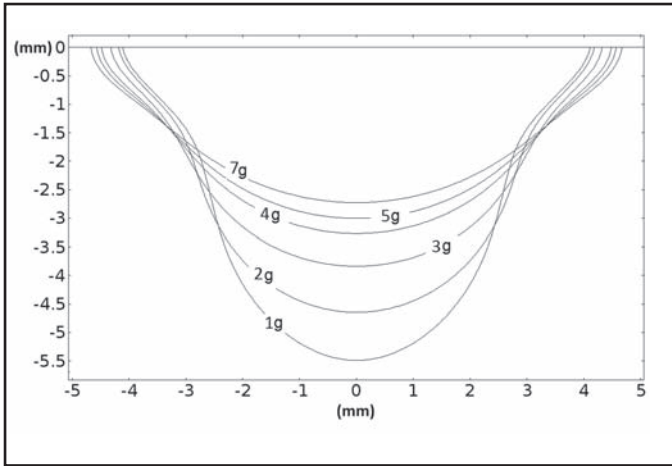


Fig. 5 — Weld pool profiles at different gravity factors.

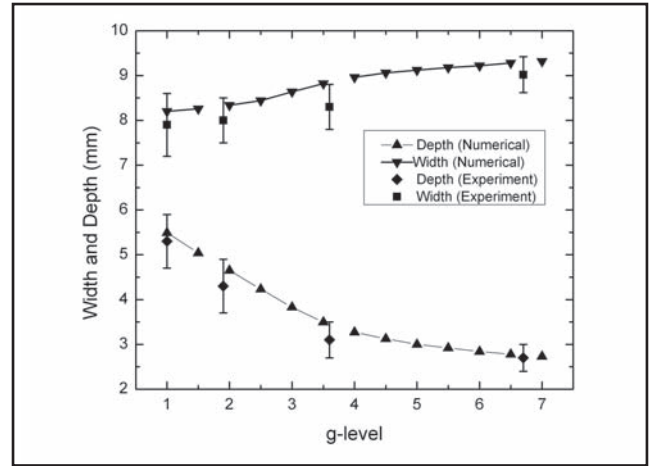


Fig. 6 — Depth and width of the weld zone.

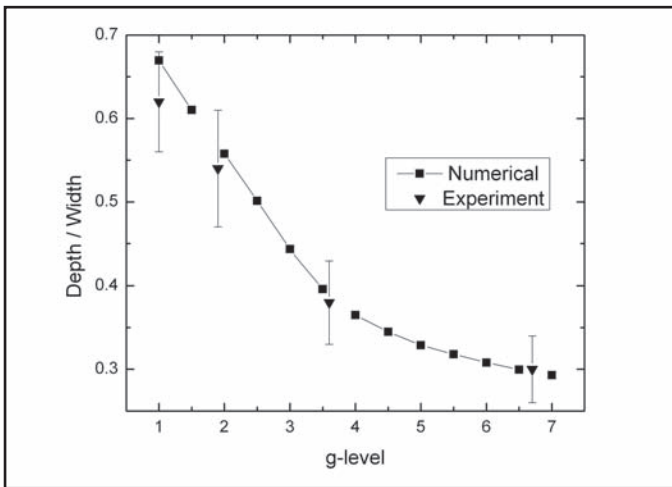


Fig. 7 — Depth-to-width ratio at different gravity factors.

For the energy equation, a Gaussian distribution of heat flux is applied to the top surface of the base metal (BM) to simulate the presence of the arc (Ref. 21), viz.,

$$q(r) = \frac{3Q}{\pi r_a^2} \exp\left(\frac{-3r^2}{r_a^2}\right) \quad (3)$$

where $Q = \eta IV$ is the heat generated by the

arc and r_a is the effective radius of the heat source. In addition, convective and radiative heat fluxes are applied to the top surface as well as all other surfaces. The convective heat transfer coefficient, surface emissivity, and ambient temperature are given in Table 1.

Numerical Method

The spot GTA welding process of 1018 steel has been simulated numerically using the finite-element software *COMSOL Multiphysics* (v.4.3a). This commercially available computational tool can handle mathematical models of physical phenomena that require the solution of a system of coupled partial differential equations. The Electric Current module in *COMSOL* is used to predict the current density distribution. The predicted current density is used in the Magnetic Field module to calculate the magnetic flux density and

Lorentz force. Finally, the Non-Isothermal Flow module is applied to solve for the velocity and temperature fields; the gravity-induced buoyancy and Lorentz forces are added to the fluid flow model as source terms and Marangoni effect is applied to the top surface as a “weak form contribution” (Ref. 24). The discretization of the fluid flow is set to P2+P1, which means quadratic for velocity and linear for pressure. The discretization for the heat transfer is set to quadratic. A very fine unstructured triangular mesh with maximum element size of 0.05 mm was applied to the weld pool domain while the mesh in the solid domain is coarser with maximum element size of 0.5 mm. The total number of triangular elements is 11,941 with an average element quality of 0.979. A fully coupled time-dependent solver with maximum time step of 0.1 s was used to solve the system of equations. The simulations were repeated for different gravity levels using a parametric sweep capability. This capability helps significantly in postprocessing the computational results.

Experimental Procedure

High-gravity environments were performed in the Clarkson University experimental facility with the multigravity research welding system (MGRWS) — Fig. 3. The MGRWS, with an arm length of 1.15 m, is capable of rotating up to 86 rev/min, which imposes a g' of 10 g ($1 \text{ g} = 9.81 \text{ m/s}^2$) on the test specimen. The welding box is pivoted to the arm so that g' is always perpendicular to the bottom of the box or the workpiece.

Samples of 1018 steel in the size of $25.4 \times 25.4 \times 6.3 \text{ mm}$ were prepared. Table 2 itemizes the composition of 1018 steel used in this study. Coupons were polished and cleaned with acetone prior to welding. The samples were subjected to the spot GTA process with the parameters listed in Table 3.

Table 3 — Spot GTAW Parameters

Arc voltage	12 V
Arc current	150 A (DCEN)
Shielding gas	Pure argon (14 L/min)
Electrode	W+2%ThO ₂ , 2.4 mm, flat tip
Electrode extension	5 mm
Arc length	3 mm
Arc time	15 s
Gravity levels	1 g, 1.9 g, 3.6 g, 6.7 g

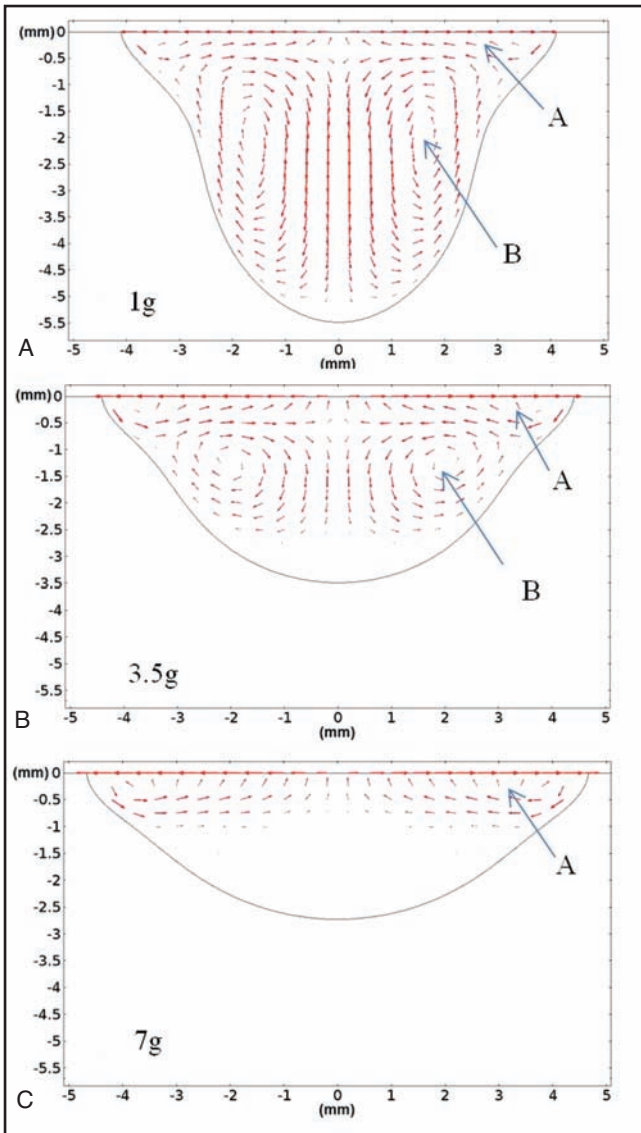


Fig. 8 — Velocity field in the weld pool for three gravity levels: A — 1 g; B — 3.5 g; C — 7 g.

After loading the sample into the sample holder, the MGRWS was first brought up to the rotation speed of interest, i.e., the speed that provided the desired g-level (g'). At this moment, the arc was turned on and a spot weld at the center of the sample was performed for an arc time of 15 s. The machine continued to rotate at the set rev/min for an additional 5 s to allow for solidification and cooling under the same condition. Subsequently, the system was brought to rest to extract the workpiece. The welding experiment was performed for four simulated gravity levels as indicated in Table 3.

The welded samples were sectioned by a diamond saw, polished, and macroetched for evaluating the WZ profile. The WZ was photographed using a 20× stereomicroscope. The depth (d) and width (w) of the WZ were accurately measured using ImageJ software.

temperatures. The experimental result for the first case (gravity level of 1 g) is used to calibrate the arc efficiency in all numerical simulations. Both numerical and experimental data show that the depth of penetration decreases as the gravity level increases. In the arc welding process, the Lorentz force is the only centrally inward force and, hence, is responsible for deepening the WZ. As gravity increases the buoyancy force decreases the deepening effect of the Lorentz force. As a result, lower penetration is expected as g increases. The results also show that the width of the WZ increases as the gravity level increases. Although the depth of penetration changes considerably with gravity, the changes in the width of the WZ are relatively small. This is because the effect of buoyancy, even though it tends to enhance slightly the relatively strong Marangoni effect, it is the

Results and Discussion

Welding of 1018 steel was experimentally examined and numerically simulated at several gravity levels. The characteristic parameters associated with both the experimental tests and computational simulations are summarized in Tables 1 and 3.

The comparison between the WZ geometry of the experimental study and numerical simulations for different g levels is presented in Fig. 4. The two lines on the left-hand side of these figures correspond to the solidus and liquidus

Marangoni effect that tends to dominate the flow near the surface of the weld pool.

Figure 5 is a schematic of WP profiles for different levels of gravity. Note that the effect of gravity on the shape of the WP is significant up until the gravity factor of 4 (4g). At gravity factors higher than 4 the shape of the WP does not change drastically with gravity.

Figure 6 illustrates the changes in the depth and width of the WP with different g levels. The results show that the numerical simulations tend to overestimate the depth and the width of the WZ for all gravity levels. The assumption of Gaussian distributions of heat flux and current density, lack of accurate thermophysical properties at very high temperatures and excluding the surface deformation from the simulation are the reasons behind this fact. Note also that for the range of changes in the depth of the WZ when gravity changes from 1 to 7 g, it is almost 2.5 times larger than the changes in the width of the WZ.

Figure 7 compares the aspect ratios of the WP for different g levels. The data illustrate the fact that the depth-to-width ratio decreases 60% by increasing the gravity from 1 to 7 g. In addition, note that there is reasonable agreement between the numerical and experimental results for the aspect ratio.

The velocity fields in the WP at the time of 15 s for the gravity levels of 1 g (no rotation), 3.5 g, and 7 g are illustrated in Fig. 8. A logarithmic scale is used to size the velocity arrows; therefore, the lengths of the vectors do not represent the magnitude of the velocity. The plots illustrate that, as a result of different convective forces, two vertical structures appear; the two structures are vortex A near the surface and vortex B in the interior of the WP. At the surface of the WP, due to the Marangoni effect (with higher surface tension at the boundaries), fluid is pushed toward the corners. Accordingly, a strong

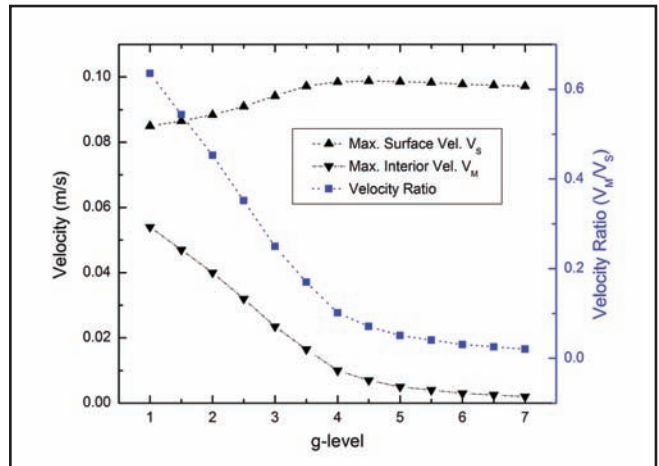


Fig. 9 — Maximum velocity inside the weld pool and on the surface, and their ratio (V_m/V_s).

centrally outward vortex (vortex A) is generated adjacent to the surface. In this vortex, the buoyancy convection and the Marangoni convection have the same direction of flow while the Lorentz force induced convection has the opposite direction of flow.

Deeper in the WP the effect of surface flow due to Marangoni convection is negligible; therefore, within the WP the Lorentz and buoyancy forces, with opposing flow directions along the centerline, determine the net fluid flow. Since the Lorentz force is dominant, a centrally downward flow is induced in the WP. The maximum speed of the molten metal near the core of vortex A at the interface is two to more than four times the maximum velocity along the centerline adjacent to the core of vortex B; the quantitative predictions of these observations are discussed in a subsequent paragraph. Although vortex B is not as strong as vortex A, vortex B covers a larger area in the interior portion of the WP, as illustrated in Fig. 8A.

By comparing the velocity fields in Fig. 8B, C, it is observed that vortex B becomes weaker at higher g levels. By increasing buoyancy force, the net driving force within the weld pool, which is the result of the two opposing forces, *viz.*, the Lorentz and the buoyancy forces, vortex B becomes weaker and the speed of the molten metal within a relatively large region near the bottom of the WP almost vanishes at highest g level.

Finally, the effect of gravity on the maximum velocity at the surface and the maximum velocity along the centerline of the WP are presented in Fig. 9. As illustrated in the figure, the maximum velocity along the centerline of the WP, V_M , decreases by increasing the gravity level. After the gravity level of 4 g , the velocity curve levels off and approaches zero; it is at this and higher g levels that the region near the bottom of the WP where the speed of the fluid is negligible. The surface velocity, V_S , increases up to a gravity factor of 4 and then starts to decrease slightly.

Conclusions

The effect of enhanced gravity on the fluid flow and heat transfer that determine the WP geometry in the spot GTA welding process of 1018 low-carbon steel was studied. The MGRWS was used to obtain experimental results while the finite-element method coded in COMSOL was applied to perform numerical simulations. Reasonable agreement of WP geometry between experimental and numerical simulations confirmed the validity of the

model. Both experimental and numerical results show wider and shallower WP profiles for higher gravity situations. It is concluded that for the cases examined in this investigation, buoyancy convection enhances the Marangoni effect (since for the welding process examined the surface tension decreases with temperature, *i.e.*, $dy/dT < 0$) and opposes the convection induced by the Lorentz force in the weld pool. In summary,

- Both numerical and experimental data show that the depth of the weld zone decreases substantially by increasing the gravity level up to 4 g ; for gravities higher than 4 g , the changes in the depth of the weld zone are insignificant.
- The maximum surface velocity increases as the gravity level increases, while the maximum velocity in the interior of the weld pool decreases at higher gravities. The rates of changes in both speeds diminish significantly for gravity levels that exceed 4 g .

References

1. Aidun, D. K., Domey, J. J., and Ahamdi, G. 2000. Effect of high gravity on weld fusion zone shape. *Welding Journal* 79(6): 145-s to 150-s.
2. Zacharia, T., Eraslan, A., Aidun, D., and David, S. 1989. Three-dimensional transient model for arc welding process. *Metallurgical and Materials Transactions B* Vol. 20B, pp. 645–659.
3. Fan, H., Tsai, H., and Na, S. 2000. Heat transfer and fluid flow in a partially or fully penetrated weld pool in gas tungsten arc welding. *International Journal of Heat and Mass Transfer* Vol. 44, pp. 417–428.
4. Zhang, W., Elmer, J. W., and DebRoy, T. 2002. Modeling and real time mapping of phases during GTA welding of 1005 steel. *Materials Science and Engineering: A* Vol. 333, pp. 320–335.
5. Goodarzi, M., Choo, R., Takasu, T., and Toguri, J. M. 1998. The effect of the cathode tip angle on the GTAW arc and weld pool: II. Mathematical model for the weld pool. *J. Phys. D: Appl. Phys.* Vol. 31 pp. 569–583.
6. Wu, C. S., Zhao, P. C., and Zhang, Y. M. 2004. Numerical simulation of transient 3-D surface deformation of completely penetrated GTA weld. *Welding Journal* 83(12): 330-s to 335-s.
7. Traidia, A., and Roger, F. 2011. Numerical and experimental study of arc and weld pool behaviour for pulsed current GTA welding. *International Journal of Heat and Mass Transfer* Vol. 54, pp. 2163–2179.
8. Tanaka, M., and Lowke, J. J. 2007. Predictions of weld pool profiles using plasma physics. *Journal of Physics D: Applied Physics* Vol. 40, pp. R1–R23.
9. Lu, F., Yao, S., Lou, S., and Li, Y. 2004. Modeling and finite element analysis on GTAW arc and weld pool. *Computational Materials Science* Vol. 29, pp. 371–378.
10. Lu, F., Tang, X., Yu, H., and Yao, S. 2006. Numerical simulation on interaction between TIG welding arc and weld pool. *Computational Materials Science* Vol. 35, pp. 458–465.
11. Traidia, A., Roger, F., and Guyot, E. 2010. Optimal parameters for pulsed gas tungsten arc welding in partially and fully penetrated weld pools. *International Journal of Thermal Sciences* Vol. 49, pp. 1197–1208.
12. Kim, W., and Na, S. 1998. Heat and fluid flow in pulsed current GTA weld pool. *International Journal of Heat and Mass Transfer* Vol. 41, pp. 3213–3227.
13. Zhang, W., Roy, G. G., Elmer, J. W., and DebRoy, T. 2003. Modeling of heat transfer and fluid flow during gas tungsten arc spot welding of low-carbon steel. *Journal of Applied Physics* Vol. 93, pp. 3022–3033.
14. Domey, J., Aidun, D., Ahmadi, G., Regel, L., and Wilcox, W. 1995. Numerical simulation of the effect of gravity on weld pool shape. *Welding Journal* 74(8): 263-s to 268-s.
15. Aidun, D., and Dean, J. 1999. Effect of enhanced convection on the microstructure of Al-Cu-Li welds. *Welding Journal* 78(10): 349-s to 354-s.
16. Voller, V., and Prakash, C. 1987. A fixed grid numerical modelling methodology for convection-diffusion mushy region phase-change problems. *International Journal of Heat and Mass Transfer* Vol. 30, pp. 1709–1719.
17. Voller, V., Brent, A. D., and Prakash, C. 1989. The modelling of heat, mass and solute transport in solidification systems. *International Journal of Heat and Mass Transfer* Vol. 32, pp. 1719–1731.
18. Voller, V. R., Brent, A. D., and Prakash, C. 1990. Modelling the mushy region in a binary alloy. *Applied Mathematical Modelling* Vol. 14, pp. 320–326.
19. Wang, R., Lei, Y., and Shi, Y. 2011. Numerical simulation of transient temperature field during laser keyhole welding of 304 stainless steel sheet. *Optics & Laser Technology* 43(4): 870–873.
20. Batchelor, G. K. 1967. *An Introduction to Fluid Dynamics*, 1st ed. New York, N.Y.: Cambridge University Press.
21. Kou, S. 2003. *Welding Metallurgy*. New Jersey: Wiley.
22. Sahoo, P., DebRoy, T., and McNallan, M. 1988. Surface tension of binary metal — Surface active solute systems under conditions relevant to welding metallurgy. *Metallurgical and Materials Transactions B* Vol. 19, pp. 483–491.
23. McNallan, M., and DebRoy, T. 1991. Effect of temperature and composition on surface tension in Fe-Ni-Cr alloys containing sulfur. *Metallurgical and Materials Transactions B* Vol. 22, pp. 557–560.
24. *COMSOL Multiphysics User's Guide*. COMSOL 4.3a, Nov. 2012.
25. Mills, K. C. 2002. *Recommended Values of Thermophysical Properties for Selected Commercial Alloys*. Cambridge, England: Woodhead Publishing.
26. Weast, R. C., Astle, M. J., and Beyer, W. H. 1985. *CRC Handbook of Chemistry and Physics*. Boca Raton, Fla.: CRC Press, Inc.